

# Pressure and thermal annealing effects on the photoconversion efficiency of polymer solar cells <sup>EP</sup>

Cite as: AIP Advances **11**, 045304 (2021); <https://doi.org/10.1063/5.0045694>

Submitted: 28 January 2021 . Accepted: 18 March 2021 . Published Online: 01 April 2021

D. O. Oyewole, <sup>ID</sup> O. K. Oyewole, K. Kushnir, T. Shi, O. V. Oyelade, <sup>ID</sup> S. A. Adeniji, <sup>ID</sup> B. Agyei-Tuffour, K. Evans-Lutterodt, <sup>ID</sup> L. V. Titova, and <sup>ID</sup> W. O. Soboyejo

## COLLECTIONS

Paper published as part of the special topic on [Chemical Physics](#), [Energy, Fluids and Plasmas](#), [Materials Science](#) and [Mathematical Physics](#)

<sup>EP</sup> This paper was selected as an Editor's Pick



View Online



Export Citation



CrossMark

## ARTICLES YOU MAY BE INTERESTED IN

[Molecular dynamics simulation on spreading of mixture nanodroplets on a smooth and homogeneous surface](#)

AIP Advances **11**, 045104 (2021); <https://doi.org/10.1063/5.0043039>

[Fabrication of a multi-stage plasma synthetic jet actuator using printed electronics](#)

AIP Advances **11**, 045105 (2021); <https://doi.org/10.1063/5.0047709>

[Flicker and random telegraph noise between gyrotropic and dynamic C-state of a vortex based spin torque nano oscillator](#)

AIP Advances **11**, 035042 (2021); <https://doi.org/10.1063/9.0000197>

AIP Advances  
**SPECIAL TOPIC:** Advances in  
Low Dimensional and 2D Materials

Call For Papers!

# Pressure and thermal annealing effects on the photoconversion efficiency of polymer solar cells

Cite as: AIP Advances 11, 045304 (2021); doi: 10.1063/5.0045694

Submitted: 28 January 2021 • Accepted: 18 March 2021 •

Published Online: 1 April 2021








View Online



Export Citation



CrossMark

D. O. Oyewole,<sup>1,2</sup> O. K. Oyewole,<sup>1,3</sup>  K. Kushnir,<sup>4</sup> T. Shi,<sup>4</sup> O. V. Oyelade,<sup>5</sup> S. A. Adeniji,<sup>5</sup>  B. Agyei-Tuffour,<sup>6</sup>   
K. Evans-Lutterodt,<sup>7</sup> L. V. Titova,<sup>4</sup>  and W. O. Soboyejo<sup>1,3,8,a)</sup> 

## AFFILIATIONS

<sup>1</sup>Materials Science and Engineering Program, Department of Mechanical Engineering, Worcester Polytechnic Institute, 100 Institute Road, Worcester, Massachusetts 01609, USA

<sup>2</sup>Physics Advanced Research Center, Sheda Science and Technology, Km 10 Abuja-Lokoja Road, P.M.B 186, Garki-Abuja, Federal Capital Territory, Nigeria

<sup>3</sup>Department of Mechanical Engineering, Worcester Polytechnic Institute, 100 Institute Road, Worcester, Massachusetts 01609, USA

<sup>4</sup>Department of Physics, Worcester Polytechnic Institute, 100 Institute Road, Worcester, Massachusetts 01609, USA

<sup>5</sup>Department of Theoretical and Applied Physics, African University of Science and Technology, Km 10, Airport Road, Galadimawa, Abuja, P.M.B. 681, Garki-Abuja, Federal Capital Territory, Nigeria

<sup>6</sup>Department of Materials Science and Engineering, School of Engineering Sciences, College of Basic and Applied Sciences, University of Ghana, P.O. Box LG 25, Legon-Accra, Ghana

<sup>7</sup>Brook-Haven National Laboratory, 98 Rochester Street, Upton, New York 11973, USA

<sup>8</sup>Department of Biomedical Engineering, Worcester Polytechnic Institute, Gateway Park Life Sciences and Bioengineering Center, 60 Prescott Street, Worcester, Massachusetts 01609, USA

<sup>a)</sup>Author to whom correspondence should be addressed: [wsoboyejo@wpi.edu](mailto:wsoboyejo@wpi.edu). Current address: Program in Materials Science and Engineering, Worcester Polytechnic Institute, 100 Institute Road, Worcester, Massachusetts 01609, USA. Tel.: +1 508 831 5448.

## ABSTRACT

This paper presents the results of experimental and theoretical studies of the effects of pressure and thermal annealing on the photo-conversion efficiencies (PCEs) of polymer solar cells with active layers that consist of a mixture of poly(3-hexylthiophene-2,5-diyl) and fullerene derivative (6,6)-phenyl-C<sub>61</sub>-butyric acid methyl ester. The PCEs of the solar cells increased from ~2.3% (for the unannealed devices) to ~3.7% for devices annealed at ~150 °C. A further increase in thermal annealing temperatures (beyond 150 °C) resulted in lower PCEs. Further improvements in the PCEs (from ~3.7% to ~5.4%) were observed with pressure application between 0 and 8 MPa. However, a decrease in PCEs was observed for pressure application beyond 8 MPa. The improved performance associated with thermal annealing is attributed to changes in the active layer microstructure and texture, which also enhance the optical absorption, mobility, and lifetime of the optically excited charge carriers. The beneficial effects of applied pressure are attributed to the decreased interfacial surface contacts that are associated with pressure application. The implications of the results are then discussed for the design and fabrication of organic solar cells with improved PCEs.

© 2021 Author(s). All article content, except where otherwise noted, is licensed under a Creative Commons Attribution (CC BY) license (<http://creativecommons.org/licenses/by/4.0/>). <https://doi.org/10.1063/5.0045694>

## I. INTRODUCTION

Organic solar cells (OSCs) have received much attention over the past three decades.<sup>1–8</sup> This is due largely to their potential for low cost processing<sup>4,9–12</sup> and applications in scenarios in which low cost, lightweight,<sup>3,13</sup> flexibility,<sup>6,13–15</sup> and stretchability<sup>16–22</sup> are important. There are also significant opportunities to laminate OSCs onto rigid or flexible substrates.<sup>23,24</sup> There is, therefore, the potential to develop low cost, lightweight, flexible/stretchable OSC structures<sup>19,20,25,26</sup> that can harness solar energy.

Since the first bi-layered OSC structures that were explored in 1986,<sup>1</sup> OSCs have been produced largely in the form of Bulk Hetero-Junction (BHJ) systems.<sup>16,27–30</sup> These consist of mixtures of electron donors and electron acceptors that improve the transport of charges across the active layers. Furthermore, most of the world record OSCs have had BHJ architectures with improved PCEs that range from 2% to 17%.<sup>28,31–33</sup> PCEs of over 17%<sup>32,33</sup> have also been achieved for BHJs by the control of active layer thickness,<sup>34,35</sup> drying time,<sup>36,37</sup> mixing ratios of donor and acceptor materials,<sup>38</sup> and solvents<sup>39</sup> used in the fabrication process. Tandem organic solar cells have also been produced with PCEs of ~17.3%.<sup>8</sup>

In any case, most of the OSCs with improved PCEs have had BHJ structures in which controlled mixtures of electron donor and acceptor materials have been used to optimize charge transport across active layers in OSCs. Using the phase diagram for poly(3-hexylthiophene-2,5-diyl) (P3HT):(6,6)-phenyl-C<sub>61</sub>-butyric acid methyl ester (PCBM) blends,<sup>40</sup> and knowledge of the crystallinity of active layers in OSCs,<sup>41–43</sup> significant improvements in PCEs have been achieved.<sup>30,41,44,45</sup> Hence, the control of annealing temperatures and the ratios of donor and acceptor materials can be used to control the blend morphologies of active layers.<sup>5,23,30,38,43,44,46</sup> The controlled annealing of BHJs can also result in the crystallization of P3HT:PCBM blends in ways that improve the overall PCEs<sup>41,42,44,45,47,48</sup> of OSCs.<sup>49</sup>

Prior work has also shown that the controlled application of pressure can be used to improve interfacial surface contacts<sup>50–55</sup> in ways that also reduce interfacial defects sizes,<sup>53</sup> which minimizes charge recombination while enhancing charge transport (across interfaces) and the PCEs of multilayered structures of solar cells.<sup>53</sup>

Earlier studies, using ultrafast optical techniques, have shown that photoexcitation of P3HT films with excess energies above the  $\pi$ - $\pi^*$  interband transition results in the direct injection of delocalized electrons and holes, followed by formation of excitons on ~1 ps timescales.<sup>56,57</sup> In P3HT-PCBM films, the distributed donor-acceptor interfaces facilitate charge transfer and dissociation of excitons, yielding additional free carriers.<sup>56–60</sup> Thus, the loss of free carriers to trapping at defects and interfaces, as well as geminate and nongeminate recombination, reduces solar cell PCEs.<sup>58,61,62</sup>

Hence, in this paper, we present the results of a combined computational and experimental study of the effects of mechanical pressure and thermal annealing on the PCEs of P3HT:PCBM BHJ solar cells. A combination of scanning electron microscopy and x-ray diffraction techniques is used to study the BHJ structures, while photoconductivity in the photoactive layers is elucidated via time-resolved Tera-Hertz (THz) spectroscopy. The current-voltage characteristics of the devices are also investigated.

Significant improvements in the PCEs of BHJ OSCs are associated with the interfacial defect length reduction due to the application of pressure during fabrication. Thermal annealing is also shown to promote the optimization of charge trapping, before discussing the implications of the results for the fabrication of OSCs.

## II. MATERIALS AND METHODS

### A. Experimental methods

Poly(3-hexylthiophene) (P3HT) consisting of 20 000 and 85 000 average  $M_w$ , fullerene derivative (6,6)-phenyl-C<sub>61</sub>-butyric acid methyl ester (PCBM), poly(3,4-ethylenedioxythiophene)-poly(styrenesulfonate) (PEDOT:PSS), anhydrous chlorobenzene, and indium tin oxide (ITO)-coated glass were all purchased from Sigma-Aldrich (Natick, MA, USA). All of the materials were used in their as received conditions. The ITO-coated glasses were patterned by etching with zinc powder and 2M hydrochloric acid. They were then washed in deionized (DI) water, before sonicating (each for 15 min) in decon-90, DI water, acetone, and isopropyl alcohol. The glass slides were blow dried using nitrogen gas. They were then treated with a UV/ozone cleaner (Novascan, Main Street Ames, IA, USA) to remove organic residuals.

Subsequently, PEDOT:PSS was filtered with a 0.45  $\mu\text{m}$  mesh filter before spin-coating with a spin coater (Laurell Technologies Corporation, North Wales, PA, USA) onto the cleaned ITO-coated glass slides at 3000 rpm for 30 s. The resulting films were annealed for 5 min at 120 °C in air before transferring them into a dry nitrogen-filled glove box. A solution of 30 mg/ml P3HT:PCBM (1:1 w/w) was then prepared by mixing 7.5 mg of 20 000  $M_w$  of P3HT and 7.5 mg of 80 000  $M_w$  of P3HT with 15 mg of PCBM in 1 ml of chlorobenzene. The solution was stirred for 2 h before filtering through a 0.2  $\mu\text{m}$  mesh filter. The solution of P3HT:PCBM blend was then spin-coated onto the PEDOT:PSS-coated ITO-glass surface at 800 rpm for 120 s. The spin-coated structure was then annealed in a dry nitrogen-filled glove box at 50 °C for 20 min. The spin coating procedures were repeated for other PEDOT:PSS/ITO-coated glasses before annealing them at different temperatures (RT = 25, 100, 150, 200, and 250 °C).

For the thermally annealed P3HT:PCBM/PEDOT:PSS/ITO-coated glass structures, a 150 nm thick aluminum layer was thermally evaporated onto P3HT:PCBM using an Edward E306A evaporation system (Edward E306A, Easton PA, USA). The evaporation was carried out at a vacuum pressure of  $\sim 1 \times 10^{-6}$  Torr at a deposition rate of 0.2 nm/s. A shadow mask was used to define a device area of 0.1  $\text{cm}^2$ .

In selected cases, a controlled mechanical pressure was applied to both the device and the P3HT:PCBM-coated glass structures using an electromechanical Instron 5848 MicroTester (Instron, 5848 MicroTester, Norwood, MA, USA) with a poly-di-methyl siloxane (PDMS) anvil, as shown in the schematics [Figs. 1(a)–1(c)]. First, the PDMS anvil was fabricated from a mixture of Sylgard 184 silicone elastomer base and Sylgard 184 silicone elastomer curing agent (Dow Corning Corporation, Midland, MI) in a ratio of 10:1 by weight. The mixture was then degassed and cured at 65 °C for 2 h in a mold with a polished silicon base. The PDMS anvil was then cut out into the dimensions of the glass substrates. Instron was used

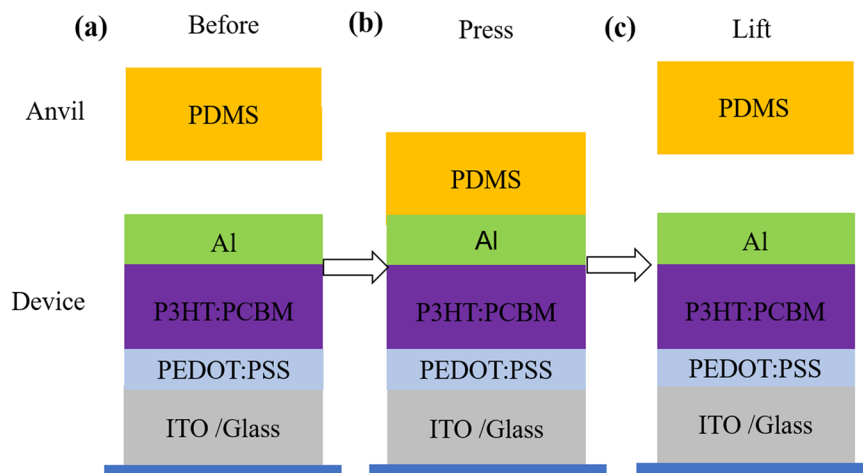


**FIG. 1.** Schematics of the pressure-assisted testing setup: (a) before pressure application, (b) during press, and (c) during lifting up of the anvil.

to apply compressive loading at a displacement rate of 1 mm/min up to a peak stress of 2 MPa. The peak stress was held constant for 10 min, before ramping down to zero stress at a displacement rate of 1 mm/min. A similar procedure was used to study the effects of ramping to peak pressures between 2 and 10 MPa.

The current density–voltage ( $J$ – $V$ ) characteristics of the fabricated devices were measured before and after the pressure treatment. This was done under AM1.5 G illumination of  $100 \text{ mW cm}^{-2}$  using a Keithley 2400 source meter unit (Keithley, Tektronix, Newark, NJ, USA) that was connected to an Oriel solar simulator (Oriel, Newport Corporation, Irvine, CA, USA). The solar simulator was calibrated using an optical power detector (918D-SL-OD2R, Newport Corporation, Irvine, CA, USA). The initial  $J$ – $V$  curves of as-prepared devices were also obtained before measuring the  $J$ – $V$  characteristics of solar cells that were subjected to pressures of 0–10 MPa.

The optical absorbances of the P3HT:PCBM blend (produced with and without pressure application) were measured using an Avantes UV-VIS spectrophotometer (Avantes, Louisville, CO, USA), before and after thermal annealing. The resulting microstructures were then observed using a field emission gun Scanning Electron Microscope (SEM) (JSM 7000F, JOEL, Ltd., Tokyo, Japan) and an Atomic Force Microscope (AFM) (Naio-AFM, Nanosurf instruments, Woburn, MA, USA).

The XRD patterns of the P3HT:PCBM-coated structures were obtained from 150 nm thick active layers (P3HT:PCBM) deposited on clean glass substrates. These were obtained using an X-Ray Diffraction (XRD) system (Malvern PANalytical, Westborough, MA, USA). XRD patterns of the P3HT:PCBM thin films were obtained (for as-prepared films at different thermal annealing conditions and those that were pressure-assisted) using a  $\text{CuK}\alpha$  radiation source with a beta nickel filter at 40 kV and 40 mA.

The influence of thermal annealing temperature and applied pressure on polymer chain alignment and crystallinity of the P3HT:PCBM films was also investigated using grazing incidence wide-angle x-ray scattering (GIWAXS) technique as previously reported.<sup>12,51</sup> The experiments were carried out using an x-ray beam of 13.5 KeV and a wavelength of 9.18 nm at the 11-BM beamline (NSLS, Brookhaven National Laboratory, USA). The films were

aligned such that the incident x-ray beam impinges on the samples at various shallow angles of  $\sim 0.05^\circ$ – $0.15^\circ$ , generating diffuse scattering from a fairly large sample volume. The GIWAXS patterns were taken from a grazing incidence of  $0.12^\circ$ , which is above the critical angle of the P3HT:PCBM blend.

Time-resolved terahertz spectroscopy (TRTS) measurements were carried out on P3HT:PCBM films that were spin-coated onto fused quartz substrates at 500 rpm for 60 s. The films were thermally annealed and assisted by mechanical pressure. The Tera-Hertz (THz) spectroscopy measurements were carried out as described previously.<sup>63–65</sup> In brief, 400 nm (or 3.1 eV), 100 fs pulses with an energy fluence of  $800 \mu\text{J}/\text{cm}^2$  were used to photoexcite the films with an optical penetration depth of P3HT:PCBM at 400 nm. These were reported as  $\sim 260 \text{ nm}$ ,<sup>59</sup> substantially smaller than the film thickness, with excitation pulses that were almost fully absorbed in all the studied films. The resulting excitation induced changes in the complex conductivity were detected using a time-delayed THz probe pulse. THz pulses with bandwidths of 0.25–2 THz (1–10 meV) were generated with an optical rectification of 100 fs and 800 nm pulses in a 1 mm thick [110] ZnTe crystal. The pulse was focused onto the P3HT:PCBM films using off-axis parabolic mirrors, and the transmitted THz pulses were detected using free-space electro-optic sampling in a second 1 mm thick [110] ZnTe crystal.

## B. Analytical and computational methods

Since excellent interfacial surface contacts are essential for the enhancement of work function alignment among the constituted layers of multilayered organic solar cells,<sup>66</sup> the interfacial surface contacts between the layers in the OSCs can be enhanced by application of pressure (compression treatment).<sup>52,66</sup> The structure and properties of thin films (subjected to mechanical pressure) also determine the deformation of the film.<sup>51</sup> Interfacial defects can also occur due to environmental or undissolved/unfiltered particles that are sandwiched between layers [as shown in Fig. S1(a) in the [supplementary material](#)]. Defects can also initiate in the photoactive layer due to surface roughness and processing conditions. Usually, the types of trapped particles vary from hard to soft/compliant materials,

depending on their Young's moduli.<sup>52</sup> These films are deformed and wrapped round the particles when pressure is applied to improve the interfacial surface contact. The deformation of a thin film around interfacial particles can be idealized by the displacement of a cantilever beam [Figs. S1(a)–S1(d)].<sup>67,68</sup> When the film deflects, the cantilever is brought into contact with the adjacent (bottom) layer. Consequently, the cantilever deflection and the interfacial surface contacts between adjacent layers provide insights into the formation of interlayer contacts between the adjacent layers of OSC structures.

However, when the trapped particles between layers are stiff (ITO, TiO<sub>2</sub>, quartz, etc.),<sup>67</sup> it is difficult to achieve interfacial layer contacts, since the void length depends on the modulus and height of the trapped particle.<sup>67</sup> Essentially, the rigid particles can sink-in into the compliant adjacent layers, which can ultimately lead to damage of the device structures. The relationship between the interfacial surface contact ( $L_c/L$ ) and the applied pressure ( $P$ ) can be expressed as<sup>51</sup>

$$\frac{L_c}{L} = 1 - \left[ \frac{3 \left( \frac{E}{1-\nu^2} \right) t^3 h}{2PL^4} \right]^{\frac{1}{4}}, \quad (1)$$

where  $L_c$  is the interfacial surface contact length,  $E$  is Young's modulus,  $\nu$  is the Poisson ratio,  $t$  is the film thickness,  $h$  is the height of the particle or film surface roughness,  $L$  is the length of the device structure, and  $P$  is the applied pressure. The relationship between the interfacial surface contact length and the defect/void dimension ( $S$ ) can be expressed as

$$\frac{S}{L} = 1 - \frac{L_c}{L}. \quad (2)$$

The materials properties of layers (Table S1) were incorporated into Eqs. (1) and (2) to estimate the interfacial surface contact lengths

and the defect/void sizes as a function of the applied pressure that can assist multilayered structures of OSCs. The detailed analytical modeling of the interfacial surface contacts is presented in the [supplementary material](#).

The interfacial surface contacts in the multilayered OSC structures were also simulated using particles of different elastic properties. The simulations utilized materials properties that have been previously reported (Table S1).<sup>18</sup> The materials properties were incorporated into finite element modeling that was carried out using the ABAQUS software package (ABAQUS, Dassault Systemes Simulia Corporation, Providence, RI, USA). The details of the simulation are presented in the [supplementary material](#).

### III. RESULTS AND DISCUSSION

#### A. Microstructures of active layers

The microstructures of as-cast and annealed photoactive layers were observed using Atomic Force Microscopy (AFM) and Scanning Electron Microscopy (SEM). It has been shown that annealing of P3HT:PCBM above the glass transition temperature of P3HT drives the diffusion of PCBM into the polymer matrix and promotes polymer self-organization and crystallization.<sup>2</sup> The glass transition temperature of P3HT has been reported to be in the range between 12 and 110 °C.<sup>2,3</sup> As the films are annealed in this temperature regime and above, the microstructures of the P3HT:PCBM films evolve with increasing annealing temperature.

The SEM images of the evolving microstructures of the annealed P3HT:PCBM films (on PEDOT:PSS/ITO-coated glasses) are presented in [Fig. 2](#). In the un-annealed film [[Fig. 2\(a\)](#)], sporadic PCBM phases were observed within the blend. Phase separation was

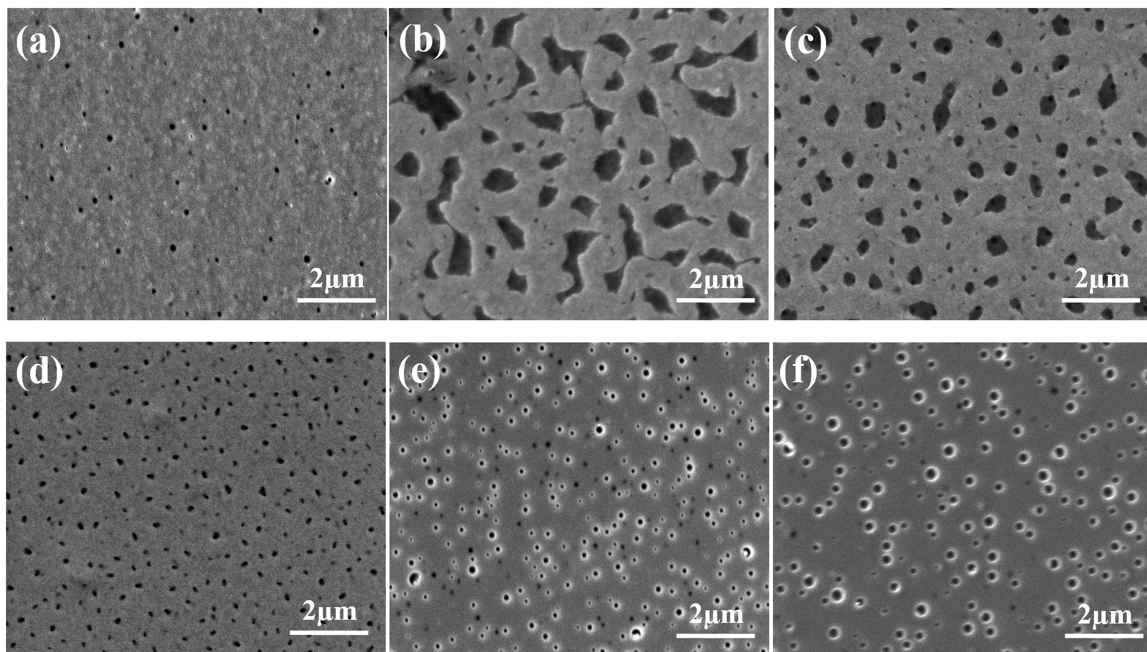


**FIG. 2.** SEM images of P3HT:PCBM films annealed at (a) room temperature (RT), (b) 50 °C, (c) 100 °C, (d) 150 °C, (e) 200 °C, and (f) 250 °C.

also observed at room temperature ( $RT = \sim 22\text{--}25^\circ\text{C}$ ). This resulted in the nucleation and growth of PCBM-rich regions in a matrix of P3HT.<sup>5</sup> For annealing temperatures of 50 and  $100^\circ\text{C}$  [Figs. 2(b) and 2(c)], phase separated domains of P3HT and PCBM were observed with micron-scale agglomeration of PCBM. However, for annealing temperatures between 100 and  $250^\circ\text{C}$ , sub-micron PCBM-rich domains were observed within the continuous P3HT matrix. The PCBM-rich domains also continued to grow by agglomeration, as the annealing temperature increased [Figs. 2(d)–2(f)]. This resulted in a larger area of P3HT-rich regions.

The above results show that increasing annealing temperatures (from 50 to  $150^\circ\text{C}$ ) enhances phase separation, yielding more finely dispersed donor and acceptor phases [Figs. 2(b)–2(d)]. This can improve transport of charges by creating percolation pathways for both donor and acceptor materials.<sup>9,35</sup> It is important to note that the P3HT:PCBM constituents attain an equilibrium morphology at  $150^\circ\text{C}$ , which is driven by the thermodynamically driven re-organization of the P3HT polymer chains and PCBM molecules. Based on the P3HT:PCBM phase diagram,<sup>40</sup> P3HT:PCBM mixtures should form a liquid phase at higher annealing temperatures of  $200\text{--}250^\circ\text{C}$  [Figs. 2(e) and 2(f)], for P3HT:PCBM ratios of 1:1 wt. %. This can lead to evaporation and the formation of pinholes at such temperatures.

The AFM images of the P3HT:PCBM films annealed at different temperatures are presented in the [supplementary material](#) [Figs. S2(a)–S2(f)]. The surface roughness values of the films are summarized in Table S2 in the [supplementary material](#). Note that the film roughness values were obtained from small areas ( $5 \times 5 \mu\text{m}^2$ ) of the film surface. The roughness of the films decreases with increasing annealing temperature, for annealing temperatures between 50 and  $150^\circ\text{C}$ . This is attributed to the effects of phase separation and the re-organization of PCBM in the P3HT matrix.<sup>4,5</sup> However, annealing at temperatures between 200 and  $250^\circ\text{C}$  results in increasing surface roughness, which can be associated with possible pinholes that were formed at high temperatures.

## B. Film crystallinity

A combination of X-Ray Diffractometry (XRD) and grazing incidence wide-angle x-ray scattering (GIWAXS) synchrotron radiation was used to study the effects of mechanical pressure and thermal annealing on the P3HT:PCBM blends. Figure 3(a) presents the XRD patterns of the films at different annealing temperatures. The intensity of the strongest peak (that corresponds to plane 100) increases with increasing temperature up to  $200^\circ\text{C}$ . Further increase in annealing temperature to  $250^\circ\text{C}$  revealed no peaks were observed due to the loss of crystallinity above the melting point. The differences in the (100) peaks of the films are clearer in the inset of Fig. 3(a). Therefore, we did not take any GIWAXS pattern measurements for the films that were annealed at  $250^\circ\text{C}$  as the XRD patterns already revealed that there were no peaks.<sup>40</sup> The strongest peaks (at  $2\theta \approx 5.3^\circ$ ) correspond to the inter-chain spacing of P3HT, which is associated with the interdigitated alkyl chains.<sup>1,2</sup> Hence, using the (100) peak, the full-width-half-maximum (FWHM) of the film was calculated using the Scherrer equation.<sup>69</sup> Table S3 presents the estimated FWHM of the films with respect to the annealing temperature. The FWHM values of the (100) peak decrease as the crystallite size increases with increasing annealing temperature up to  $200^\circ\text{C}$ .

GIWAXS patterns of the films at different annealing temperatures between 50 and  $200^\circ\text{C}$  are shown in Figs. 3(b) and 3(c) along with the GIWAXS patterns of the films that were assisted by mechanical pressures between 0 and 10 MPa [Fig. 3(d)]. There was a left shift in the peaks [Fig. 3(b)] due to increasing annealing temperature. This is associated with an increase in the quality of crystal of the films and strain relaxation between the films and the substrates. We also observed a further slight left shift in the peaks obtained for the pressure-assisted films [Fig. 3(d)]. This slight shift can also be an indication of induced-crystallization and reduction in the defects<sup>53</sup> within the films.

The two-dimensional GIWAXS images [Figs. S3(a)–S3(e)] of the films show evidence of  $\pi$ – $\pi$  stacking in the direction parallel to the substrate, that is, (100) peak along  $q_z$  and (010) being in-plane along  $q_x$ , as shown by the weak in-plane scattering at  $\sim 1.65 \text{ \AA}^{-1}$ . There is evidence of slight  $\pi$ – $\pi$  stacking in the direction that is perpendicular to the substrate, as the lamellar stacking is in-plane. In the annealed films, the  $\pi$ – $\pi$  stacking is predominantly parallel to the substrate. Annealing drives the system toward a lower free energy state by the self-organization of the P3HT lamellar and the  $\pi$ – $\pi$  stacking direction parallel to the substrate, whereby attaining an edge-on configuration.<sup>70,71</sup> The decrease in the FWHM values (Table S3) of the out-of-plane peak suggests that the P3HT lamellae/crystallites grew in a direction that was parallel to the substrate.

## C. Optical properties

The optical properties of the P3HT:PCBM films are presented in Figs. 4(a) and 4(b). We observed a significant increase in magnitude and a slight red shift of the absorbance peaks within the visible spectrum (450–650 nm) with increasing annealing temperatures between room temperature (RT) and  $200^\circ\text{C}$  [Fig. 4(a)]. This increase in absorption is associated with an increase in the packing of the P3HT chains. In the case of the films that were annealed between RT and  $150^\circ\text{C}$ , two vibronic shoulders [red triangles in Fig. 4(a)] were observed at 550 and 600 nm wavelengths. These are attributed to higher levels of crystallization [as shown in Figs. 3(a)–3(c)] by intra-chain stacking in conducting polymers.<sup>72</sup> There was pronounced blue shift of the peaks in the films annealed above  $150^\circ\text{C}$ . The disappearance of the vibronic shoulders at  $200^\circ\text{C}$  annealing temperature [Fig. 4(a)] is attributed to a low level of intra-chain stacking in the films. In the case of pressure-assisted films, there is also a significant increase in absorption of light [Figs. 4(b) and S4]. This can be associated with healing of defects within films and along the film/substrate interface. There is tendency for the film to strain horizontally as the mechanical pressure is being applied to the surface of the films, leading to closing of existing voids/defects and induced-phase separation.

## D. Photoexcitation of charge carrier generation and transport

We have used time-resolved terahertz spectroscopy (TRTS) to study the effects of microstructural changes due to mechanical pressure and thermal annealing. These reveal the intricate interplay of processes involved in the photoexcitation of P3HT:PCBM films. As the low energy THz pulses are sensitive to free, mobile charge carriers, TRTS enables contact-free, all-optical measurements of

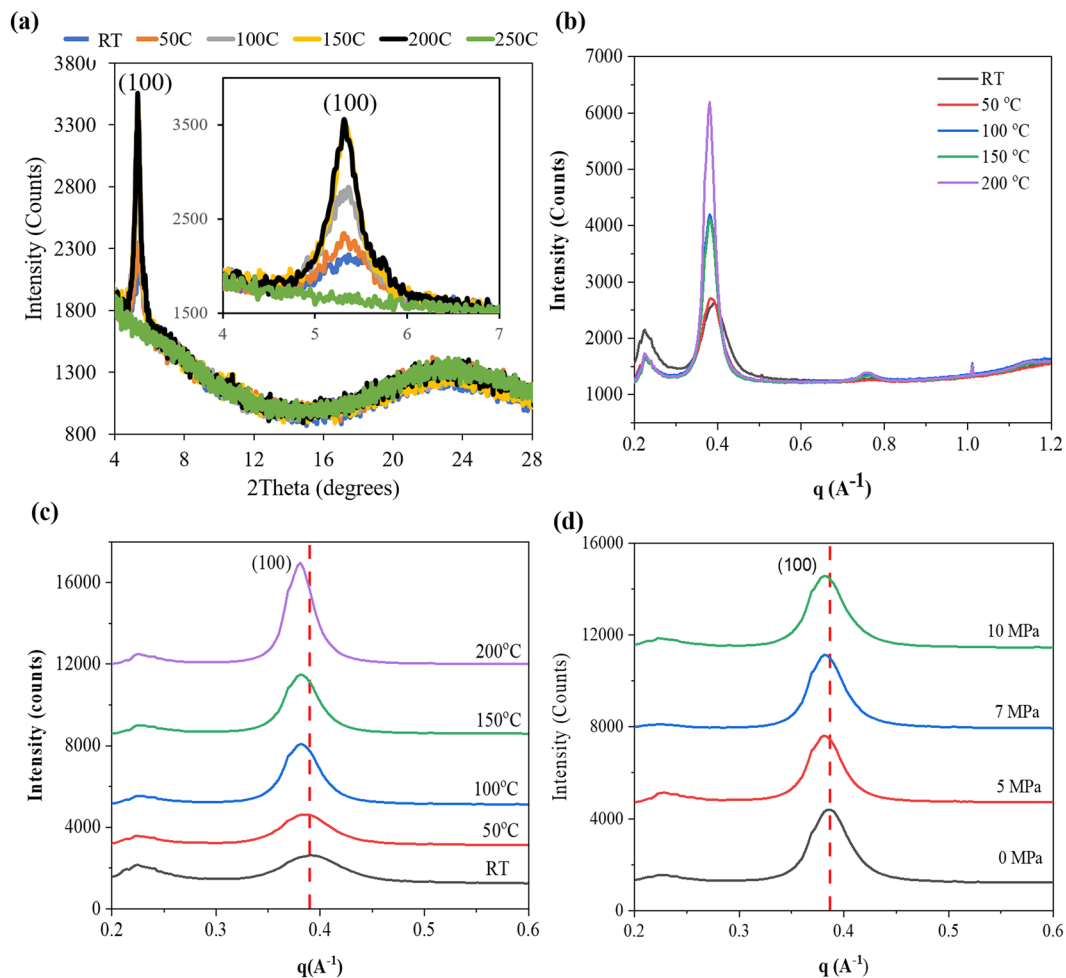


**FIG. 3.** Crystallinity of the P3HT:PCBM films: (a) XRD patterns at different annealing temperatures; (b) and (c) GIWAXS patterns at different annealing temperatures; (d) GIWAXS patterns of the pressure-assisted films.

microscopic photoconductivity and dynamics of photoexcited charge carriers. These include free carriers and charged species, such as polarons, in the case of conjugated polymers and organic semiconductors.<sup>56,59,60,73–77</sup> Monitoring the excitation—induced changes (in the THz absorption regime) as a function of the optical pump—THz probe delay provides information about the carrier lifetime and photoconductivity dynamics. In the limit of small photo-induced changes, the negative change in the transmission of the THz probe pulse peak is proportional to photoconductivity, as  $-\Delta T(t)/T \propto \Delta\sigma(t)$ .

Figures 4(c) and 4(d) summarize the transient photoconductivity dynamics in a series of films annealed at different temperatures [Fig. 4(c)] and in a series of films annealed at 150 °C that have been assisted by pressure [Fig. 4(d)]. The overall dynamics of the films agree with previously reported results on P3HT:PCBM films:<sup>56,59,60,77,78</sup> a rapid increase in photoconductivity over timescales that are comparable to or shorter than our experimental time resolution of  $\sim 200$  fs is followed by a multi-exponential

decrease that in the experimental time window is well-described by a biexponential decay function  $\Delta\sigma(t) = A_1 e^{-t/\tau_1} + A_2 e^{-t/\tau_2} + y_0$ . In this function,  $A_1, A_2$  represent amplitudes of the two constituent decay components and  $y_0$  is a constant offset that represents a longer-lived component that decays over the timescales that are longer than 20 ps. The fastest,  $\tau_1 = 0.5 \pm 0.1$  ps, decay component is consistent with exciton formation time, while a slower,  $\tau_2 = 4 \pm 1$  ps, component likely accounts for trapping of free carriers at defects and grain boundaries. A fraction of charge carriers remains free and mobile for considerably longer times and is represented by the constant offset  $y_0$ .

While the fast and slow decay times are essentially unchanged by thermal annealing or pressure, the overall magnitude of photoconductivity is sensitive to both. With the same film thicknesses in both series and the same excitation conditions, this change in overall peak photoconductivity can be explained by differences in the density of free carriers that is present in the films at times longer than an experimental time resolution of  $\sim 200$  fs and, to a

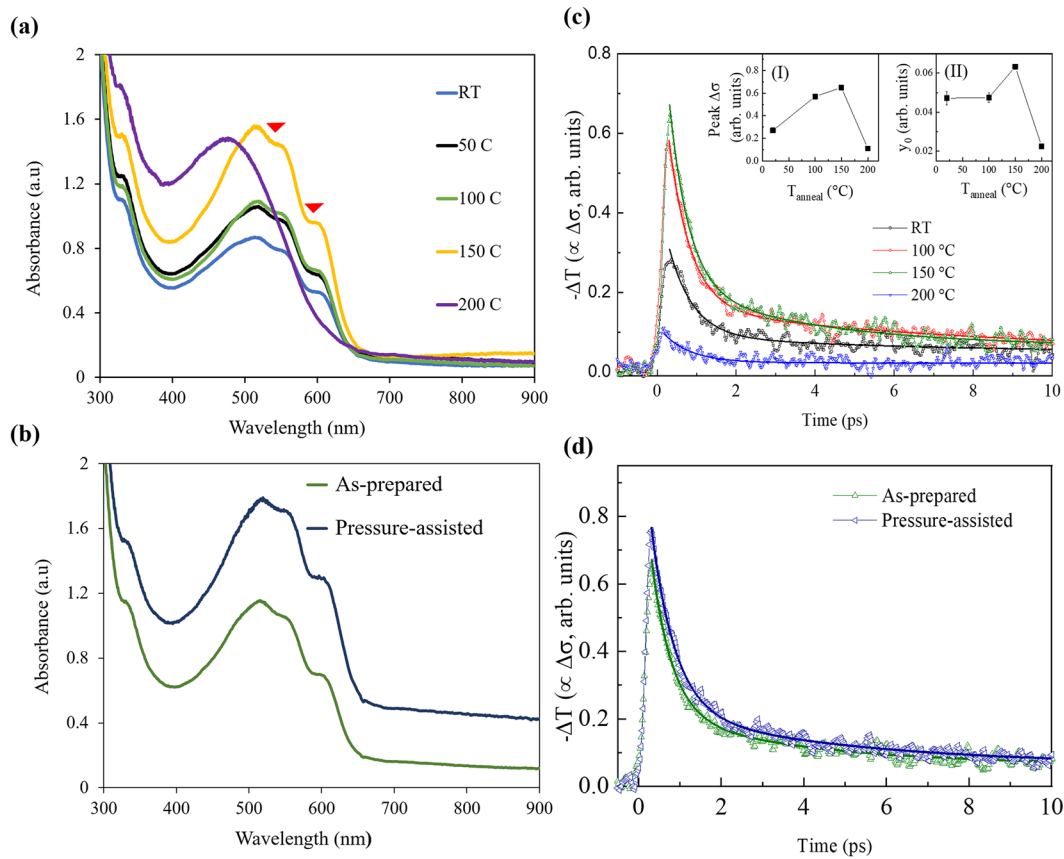


**FIG. 4.** Optical absorbance spectra and transient photoconductivity of P3HT:PCBM films: (a) optical absorbance at different annealing temperatures (the red triangles indicate the positions of two vibronic shoulders at around 550 nm and 600 nm); (b) optical absorbance of pressure-assisted films that were thermally annealed at 100 °C; (c) transient photoconductivity ( $-\Delta T \propto \Delta\sigma$ ) following excitation with 400 nm, 100 fs pulses with  $\sim 800 \mu\text{J}/\text{cm}^2$  fluence for films prepared with different annealing temperature (insets I and II show the peak photoconductivity and the long-lived photoconductivity component as a function of the annealing temperature, respectively); (d) transient photoconductivity for pressure-assisted films annealed at 150 °C.

lesser extent, by annealing-induced and pressure-induced changes in carrier mobility, discussed in more detail below. Insets I and II in Fig. 4(c) show the dependence of peak photoconductivity and long-lived photoconductivity ( $\gamma_0$ ) on annealing temperature. Both parameters increase in films with increasing annealing temperatures up to  $\sim 150^\circ\text{C}$ , where microstructure changes observed in SEM [Figs. 2(a)–2(f)] and AFM [Figs. S2(a)–S2(f)] images demonstrate improvements of crystallinity, reduction of surface roughness, and formation of percolative pathways for both electrons (in continuous PCBM domains) and holes (in the P3HT matrix). Improvement in peak photoconductivity can likely be attributed to suppressed trapping and self-localization of the free carriers over short ( $< 200$  fs) timescales at defect sites. However, when annealing temperature is increased to 200 °C, both peak and long-lived photoconductivity drop, consistent with the reduction of light absorption [Fig. 4(a)] due to the formation of pin holes [Fig. 2(e)] at high annealing temperatures. Applying mechanical pressure to the films annealed at 150 °C further improved photoconductivity.

For more insight into microscopic conductivity of films and influence of thermal annealing and mechanical pressure on carrier mobility, we have recorded complex frequency-resolved photoconductivity spectra at 2–3 ps after photoexcitation (Fig. S5). Complex photoconductivity spectra were calculated by analyzing the photoexcitation-induced changes in the amplitude and the phase of the THz pulse waveform transmitted through the sample.<sup>79,80</sup> We then model complex photoconductivity of P3HT:PCBM films with a phenomenological Drude–Smith model,<sup>81,82</sup> a modification of the free carrier Drude conductivity that accounts for localization of the mobile carriers on the length scales commensurate with their mean free path and has been extensively applied to describe photoconductivity in conjugated polymers and other disordered systems.<sup>56,57,59,60,73,78</sup> See the [supplementary material](#) for the details of the Drude–Smith model. Results from the analysis of the Drude–Smith analysis are presented in Fig. S5 for both thermally annealed [Fig. S5(a)] and pressure-assisted [Fig. S5(b)] films. The long-range conductivity ( $\sigma_{DS}$ ) of the polymeric films is also presented in Fig. S6(a).



Furthermore, using the Drude–Smith momentum relaxation time,  $\tau_{DS}$  (an experimental fitting parameter), and an effective mass  $m^* = 1.7m_e$ ,<sup>83</sup> we can calculate both the short-range ( $\mu_{short-range}$ ) mobility of carriers within the homogenous and the long-range mobility ( $\mu_{long-range}$ ) over macroscopic length scales. See details in the [supplementary material](#). Dependence of both of these parameters on annealing temperature and mechanical pressure is also shown in Figs. S6(b) and S6(c). We find that short range mobility is in good agreement with a theoretical prediction of  $31 \text{ cm}^2/\text{Vs}$  for crystalline P3HT.<sup>83</sup> Long range mobility of the free carriers is significantly lower, limited by the size of the crystalline regions and transport of carriers through the grain boundaries. We find that both short-range mobility and long-range mobility increase slightly in response to thermal annealing, which improves crystallinity and grows percolative pathways.

### E. Performance characteristics of devices

The current density–voltage (J–V) curves are presented in Fig. 5(a) for as-prepared P3HT:PCBM devices that were annealed at different temperatures (RT–250 °C). The device parameters (fill

**TABLE I.** Summary of device parameters: short-circuit current density ( $J_{sc}$ ), open circuit voltages ( $V_{oc}$ ), fill factors (FFs), and photo-conversion efficiencies (PCEs) at different annealing temperatures.

Temperature (°C)	$J_{sc}$ ( $\text{mA cm}^{-2}$ )	$V_{oc}$ (V)	FF	PCE <sup>a</sup> (%)
RT	6.16	0.8	0.42	2.32
50	6.37	0.76	0.52	2.52
100	7.37	0.74	0.44	2.70
150	10.62	0.75	0.42	3.70
200	1.26	0.69	0.26	0.25
250	0.50	0.33	0.15	0.03

<sup>a</sup>Average values of PCEs from five to eight devices.

factors, FFs; short-circuit current densities,  $J_{sc}$ ; open circuit voltages,  $V_{oc}$ ; and PCE) are summarized in Table I. The results show increased PCEs with increasing temperatures between RT and 150 °C. However, annealing at higher temperatures (200 and 250 °C) leads to reduced OSC performance characteristics. The J–V curves of the pressure-assisted devices are also presented in Figs. 5(b)

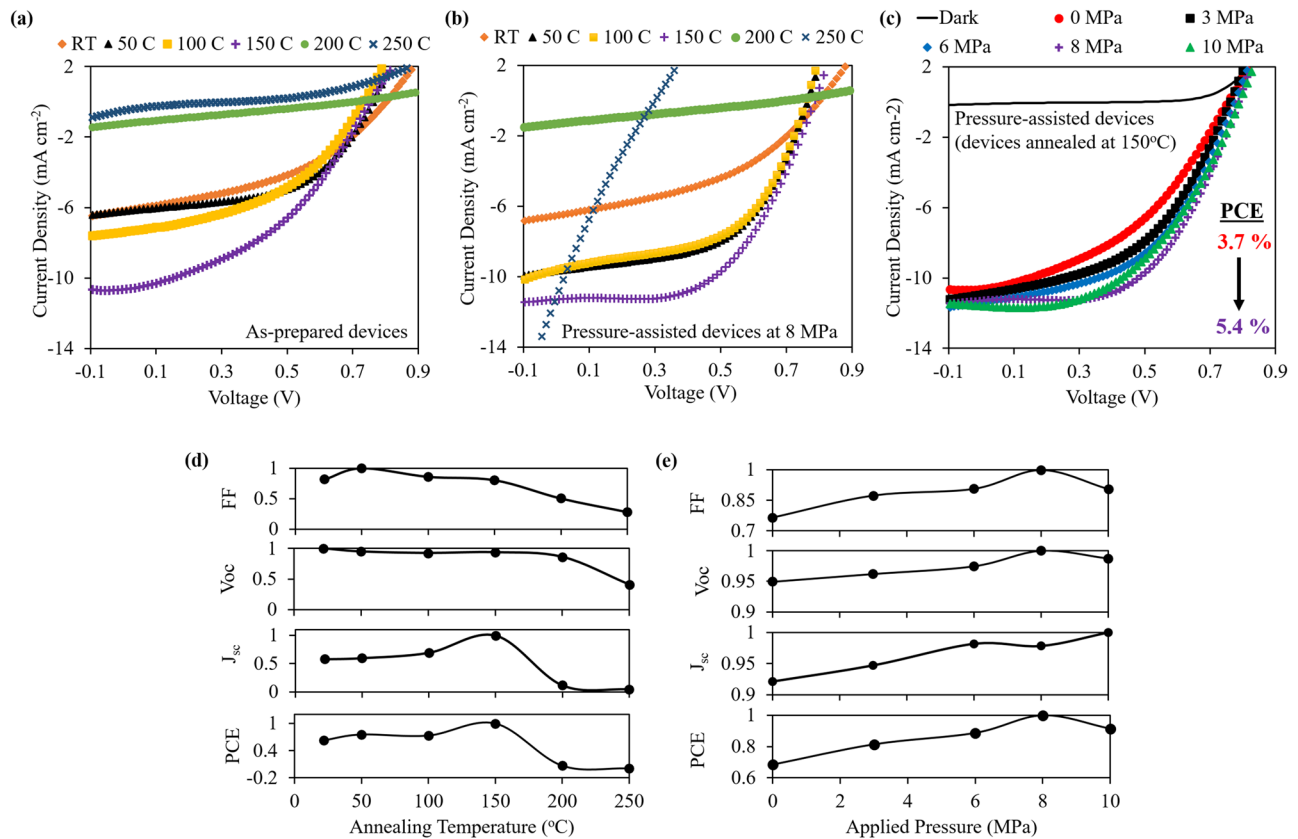


**FIG. 5.** Characteristics performance of OSCs at different applied pressures and thermal annealing temperatures: (a) current density–voltage curves of as-prepared devices at different thermal annealing temperatures; (b) current density–voltage curves of pressure-assisted devices (for 8 MPa applied pressure) at different thermal annealing temperatures; (c) effects of pressure on the current density–voltage curves of devices at 150 °C annealing temperature; (d) normalized device characteristic parameters vs annealing temperature; (e) normalized device characteristic parameters vs applied pressure.

**TABLE II.** Summary of device parameters at different applied pressures.

Pressure (MPa)	$J_{sc}$ (mA cm <sup>-2</sup> )	$V_{oc}$ (V)	FF	PCE <sup>a</sup> (%)
0	10.62	0.75	0.42	3.70
2	10.92	0.76	0.48	4.41
5	11.32	0.77	0.50	4.80
8	11.28	0.79	0.55	5.41
10	11.53	0.78	0.50	4.95

<sup>a</sup> Average values of PCEs from four to six devices.

and 5(c), while a summary of the pressure effects on device parameters is presented in Table II. The results show an increased PCE with increasing applied pressure between 0 and 8 MPa for all devices annealed at different temperatures [Fig. 5(b)]. However, the application of pressure to devices that were prepared at higher temperatures (above 150 °C) resulted in almost linear J–V curves [Fig. 5(b)].

In the case of devices that were thermally annealed at 150 °C, pressure application significantly increased PCEs by ~46% [as shown in Fig. 5(c)]. The normalized device parameters are presented in Figs. 5(d) and 5(e) for different annealing temperatures [Fig. 5(d)]

and applied pressures [Fig. 5(e)]. Both the PCEs and short circuit current densities ( $J_{sc}$ ) of devices increased with increasing annealing temperature between RT and 150 °C, while there were no significant improvements in the open circuit voltage ( $V_{oc}$ ) and fill factor (FF) [Fig. 5(d)] with increasing annealing temperature. For the devices annealed at 150 °C, the normalized device parameters (PCE,  $J_{sc}$ ,  $V_{oc}$ , and FF) increased with increasing applied pressure between 0 and 8 MPa [Fig. 5(e)].

The above trends in the device performance characteristics are attributed to the combined effects of improved crystallinity, enhanced photoconductivity, and reduced defects in layers and along interfaces of multilayered structures. Applied pressures close up voids within the device active layer and improve interfacial surface contacts, which reduces trapping of carriers and layer and interfacial defects. Hence, annealing at temperatures up to 150 °C improves charge transport in OSCs,<sup>6</sup> while applied pressure reduces defect lengths and enhances charge transport<sup>51</sup> across interfaces in BHJ structures.

Hence, the improvements in photoconversion efficiencies due to mechanical pressure and thermal annealing effects are attributed to the improved P3HT:PCBM film texture and interfacial surface contacts. The decrease in device performance, for pressure

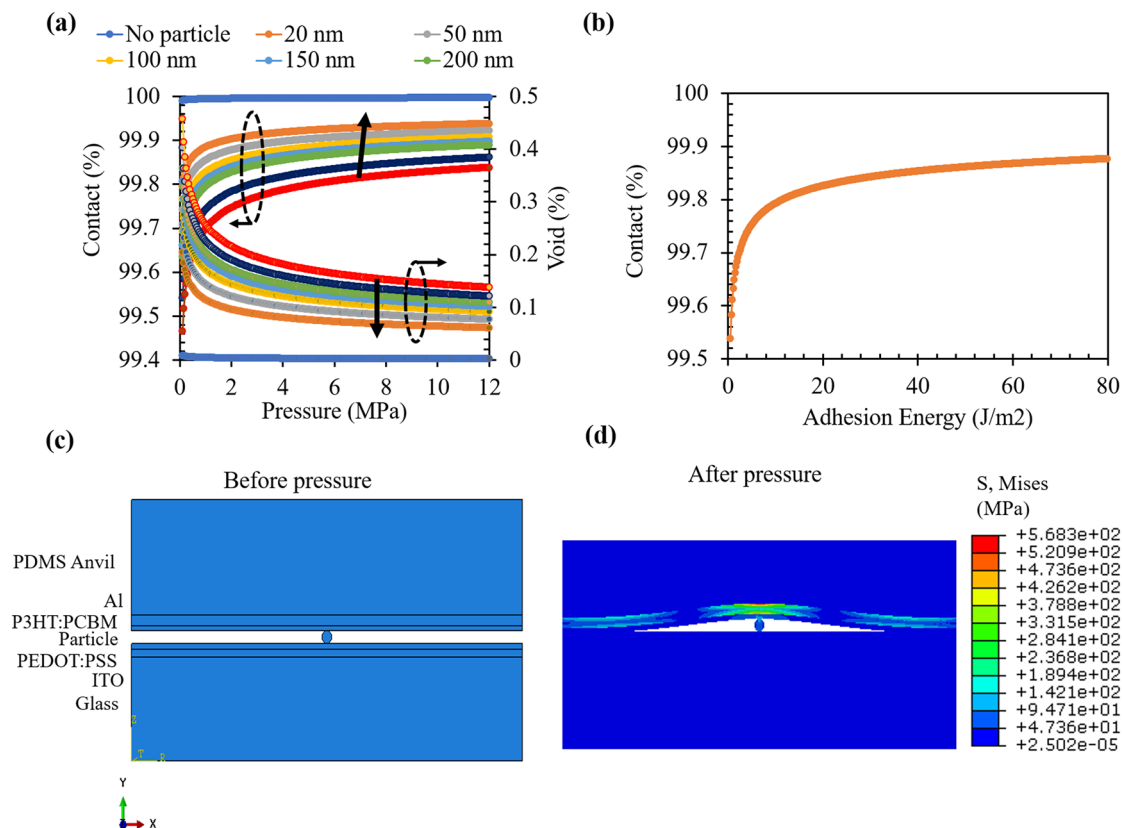


**FIG. 6.** Modeling of effects of mechanical pressure on interfacial surface contacts: (a) analytical modeling of interfacial surface contacts and voids vs pressure for particles of different sizes; (b) interfacial surface contact vs adhesion energy; (c) and (d) computational modeling of interfacial surface contacts before (c) and after (d) pressure application. The modeling considers the interface between P3HT:PCBM and PEDOT:PSS of the device.

application above  $\sim 8$  MPa, is attributed to the sink-in of impurities that are present at the interfaces between the layers<sup>51,52,84</sup> or inclusions at the defect sites. Such sink-in phenomena have been modeled in prior work<sup>53</sup> and shown to promote “damage phenomena” that decrease the device performance, in cases where the applied pressures exceed  $\sim 8$  MPa.

#### F. Effects of pressure on interfacial defects

We elucidated the effects of mechanical pressure on interfacial defects using analytical and computational modeling. The estimated interfacial surface contact lengths (for different sizes of the particles) are presented in Fig. 6(a) as a function of the applied pressure. The P3HT:PCBM photoactive layer showed an improved interfacial surface contacts with increasing applied pressures [Fig. 6(a)]. The presence of defects/voids also reduces with the increased pressure. The surface contact lengths and voids between the active P3HT:PCBM layer and the adjacent layers were calculated at different applied pressures between 0 and 12 MPa [using Eqs. (1) and (2)]. As expected, the results showed increased contacts as the interfacial adhesion energy increased [Fig. 6(b)]. More results on the improved interfacial surface contacts between the different layers of OSCs are presented in Figs. S7(a)–S7(d) in the supplementary material. The results also show that, for small particle sizes, OSC films require less pressure for surface contact to occur between adjacent layers compared to large particle sizes.

We simulated the interfacial surface contacts using the ABAQUS software package (ABAQUS, Pawtucket, RI, USA). The detailed finite element analysis (FEA) is presented in Fig. S8. Our results of the simulated interfacial contacts between the photoactive layer and the hole-transporting layer (PEDOT:PSS), before and after pressure application, are presented in Figs. 6(c) and 6(d). The PDMS anvil deforms and curls around the particle as the surface contact increases. It is important to note that interfacial surface contacts depend on mechanical properties of particles. Compliant particles deform very easily with increasing pressure, compared to the limited deformation of rigid particles. The distribution of stresses in the structures is lower for compliant particles (with better interfacial surface contacts) compared with that of rigid particles [as shown in Figs. S9(a)–S9(d)].

#### IV. CONCLUSIONS

This paper explores the effects of pressure application and thermal annealing on the structure and performance characteristics of polymer solar cells with blended P3HT:PCBM active layers. The results show that thermal treatment at temperatures up to  $150^\circ\text{C}$  enhances the agglomeration of PCBM-rich domains in the active material, P3HT:PCBM, of the OSCs. These structural changes lead to improved optical absorption, increased mobility, and increased lifetime of the optically excited charge carriers and, as a result, to an increase in the PCEs of the solar cells from  $\sim 2.3\%$  for cells annealed at room temperature to  $3.7\%$  for solar cells annealed at  $150^\circ\text{C}$ . At higher annealing temperatures, the crystallinity decrease, accompanied by pinhole formation, results in a decrease in photoconductivity and the degradation of the PCEs of the OSCs. The application of pressure (up to pressures of  $\sim 8$  MPa) also increases the device PCEs from  $3.8\%$  to  $5.4\%$ . This improvement is attributed to the reduction

in interfacial defect sizes due to pressure application. At pressures beyond 8 MPa, the induced damage (sink-in) of the OSC structures results in a reduction in PCEs.

#### SUPPLEMENTARY MATERIAL

See the [supplementary material](#) for schematics of the analytical modeling of interfacial surface contacts, computational modeling of interfacial surface contacts, additional results of characterization of P3HT:PCBM films, Drude–Smith model of terahertz photoconductivity of films, additional results of interfacial surface contact modeling, FEA model for the pressure treatment of OSCs, and effects of pressure on interfacial surface contacts for particles of different elastic properties.

#### ACKNOWLEDGMENTS

The authors acknowledge the Pan African Materials Institute of the World Bank African Centers of Excellence Program (Grant No. P126974) and the Worcester Polytechnic Institute for financial support. The authors also appreciate the African University of Science and Technology (AUST) for their financial support.

#### DATA AVAILABILITY

The data that support the findings of this study are available from the corresponding author upon reasonable request.

#### REFERENCES

- 1 C. W. Tang, “Two-layer organic photovoltaic cell,” *Appl. Phys. Lett.* **48**, 183–185 (1986).
- 2 S. D. Yambem, K. S. Liao, and S. A. Curran, “Enhancing current density using vertically oriented organic photovoltaics,” *Sol. Energy Mater. Sol. Cells* **101**, 227–231 (2012).
- 3 M. Kaltenbrunner *et al.*, “Ultrathin and lightweight organic solar cells with high flexibility,” *Nat. Commun.* **3**, 770 (2012).
- 4 F. Aziz and A. F. Ismail, “Spray coating methods for polymer solar cells fabrication: A review,” *Mater. Sci. Semicond. Process.* **39**, 416–425 (2015).
- 5 A. Facchetti, “Polymer donor-polymer acceptor (all-polymer) solar cells,” *Mater. Today* **16**, 123–132 (2013).
- 6 G. Li, R. Zhu, and Y. Yang, “Polymer solar cells,” *Nat. Photonics* **6**, 153–161 (2012).
- 7 F. C. Krebs, “Fabrication and processing of polymer solar cells: A review of printing and coating techniques,” *Sol. Energy Mater. Sol. Cells* **93**, 394–412 (2009).
- 8 L. Meng, Y. Zhang, X. Wan, C. Li, X. Zhang, Y. Wang, X. Ke, Z. Xiao, L. Ding, R. Xia, H. L. Yip, Y. Cao, and Y. Chen, “Organic and solution-processed tandem solar cells with 17.3% efficiency,” *Science* **361**, 1094–1098 (2018).
- 9 H. Hoppe and N. S. Sariciftci, “Organic solar cells: An overview,” *J. Mater. Res.* **19**, 1924–1945 (2004).
- 10 F. C. Krebs, M. Jørgensen, K. Norrman, O. Hagemann, J. Alstrup, T. D. Nielsen, J. Fyenbo, K. Larsen, and J. Kristensen, “A complete process for production of flexible large area polymer solar cells entirely using screen printing-First public demonstration,” *Sol. Energy Mater. Sol. Cells* **93**, 422–441 (2009).
- 11 R. Zhang, K.-S. Moon, W. Lin, J. C. Agar, and C. P. Wong, “A simple, low-cost approach to prepare flexible highly conductive polymer composites by *in situ* reduction of silver carboxylate for flexible electronic applications,” *Compos. Sci. Technol.* **71**, 528–534 (2011).
- 12 C. Sun *et al.*, “A low cost and high performance polymer donor material for polymer solar cells,” *Nat. Commun.* **9**, 743 (2018).

- <sup>13</sup>Y. Liu, N. Qi, T. Song, M. Jia, Z. Xia, Z. Yuan, W. Yuan, K.-Q. Zhang, and B. Sun, "Highly flexible and lightweight organic solar cells on biocompatible silk fibroin," *ACS Appl. Mater. Interfaces* **6**, 20670–20675 (2014).
- <sup>14</sup>J. Asare, B. Agyei-Tuffour, O. K. Oyewole, G. M. Zebaze-Kana, and W. O. Soboyejo, "Deformation and failure of bendable organic solar cells," *Adv. Mater. Res.* **1132**, 116–124 (2015).
- <sup>15</sup>T. Kim *et al.*, "Flexible, highly efficient all-polymer solar cells," *Nat. Commun.* **6**, 8547 (2015).
- <sup>16</sup>D. J. Lipomi, B. C. K. Tee, M. Vosgueritchian, and Z. Bao, "Stretchable organic solar cells," *Adv. Mater.* **23**, 1771–1775 (2011).
- <sup>17</sup>Y.-T. Hsieh, J.-Y. Chen, C.-C. Shih, C.-C. Chueh, and W.-C. Chen, "Mechanically robust, stretchable organic solar cells via buckle-on-elastomer strategy," *Org. Electron.* **53**, 339–345 (2018).
- <sup>18</sup>O. K. Oyewole, *Effects of Adhesion and Deformation on Stretchable Electronic Structures* (African University of Science and Technology, 2015).
- <sup>19</sup>O. K. Oyewole, D. O. Oyewole, J. Asare, B. Agyei-Tuffour, M. G. Zebaze Kana, and W. O. Soboyejo, "Failure mechanisms in layers relevant to stretchable organic solar cells," *Adv. Mater. Res.* **1132**, 106–115 (2015).
- <sup>20</sup>O. Oyewole *et al.*, "Failure of stretchable organic solar cells under monotonic and cyclic loading," *Macromol. Mater. Eng.* **305**, 2000369 (2020).
- <sup>21</sup>O. K. Oyewole *et al.*, "Micro-wrinkling and delamination-induced buckling of stretchable electronic structures," *J. Appl. Phys.* **117**, 235501 (2015).
- <sup>22</sup>O. K. Oyewole, D. O. Oyewole, M. G. Zebaze Kana, and W. O. Soboyejo, "Reliability and physics failure of stretchable organic solar cells," *MRS Adv.* **1**, 21–26 (2016).
- <sup>23</sup>O. K. Oyewole *et al.*, "Lamination of organic solar cells and organic light emitting devices: Models and experiments," *J. Appl. Phys.* **118**, 075302 (2015).
- <sup>24</sup>J. Asare *et al.*, "Effects of pre-buckling on the bending of organic electronic structures," *AIP Adv.* **7**, 045204 (2017).
- <sup>25</sup>J. Asare, B. Agyei-Tuffour, O. K. Oyewole, V. C. Anye, D. Y. Momodu, G. M. Zebaze-Kana, and W. O. Soboyejo, "Effects of deformation on failure mechanisms and optical properties of flexible organic solar cell structures," *Adv. Mater. Res.* **1132**, 125–143 (2015).
- <sup>26</sup>O. K. Oyewole, J. Asare, D. O. Oyewole, B. Agyei-Tuffour, V. C. Anye, M. G. Zebaze Kana, and W. O. Soboyejo, "Effects of adhesion and stretching on failure mechanisms and optical properties of organic solar cells," *Adv. Mater. Res.* **1132**, 89–105 (2015).
- <sup>27</sup>A. Venkateswararao, S. W. Liu, and K. T. Wong, "Organic polymeric and small molecular electron acceptors for organic solar cells," *Mater. Sci. Eng., R* **124**, 1–57 (2018).
- <sup>28</sup>K. L. Jae *et al.*, "Processing additives for improved efficiency from bulk heterojunction solar cells," *J. Am. Chem. Soc.* **130**, 3619–3623 (2008).
- <sup>29</sup>J. Kim, K. Kim, S. Hwan Ko, and W. Kim, "Optimum design of ordered bulk heterojunction organic photovoltaics," *Sol. Energy Mater. Sol. Cells* **95**, 3021–3024 (2011).
- <sup>30</sup>O. Akogwu, W. Akande, T. Tong, and W. Soboyejo, "Dendrite growth in annealed polymer blends for use in bulk heterojunction solar cells," *J. Appl. Phys.* **110**, 103517 (2011).
- <sup>31</sup>W. Zhao, S. Li, H. Yao, S. Zhang, Y. Zhang, B. Yang, and J. Hou, "Molecular optimization enables over 13% efficiency in organic solar cells," *J. Am. Chem. Soc.* **139**, 7148–7151 (2017).
- <sup>32</sup>Y. Lin *et al.*, "17.1% efficient single-junction organic solar cells enabled by n-type doping of the bulk-heterojunction," *Adv. Sci.* **7**, 1903419 (2020).
- <sup>33</sup>Q. An *et al.*, "Alloy-like ternary polymer solar cells with over 17.2% efficiency," *Sci. Bull.* **65**, 538–545 (2020).
- <sup>34</sup>T. Kirchartz, T. Agostinelli, M. Campoy-Quiles, W. Gong, and J. Nelson, "Understanding the thickness-dependent performance of organic bulk heterojunction solar cells: The influence of mobility, lifetime, and space charge," *J. Phys. Chem. Lett.* **3**, 3470–3475 (2012).
- <sup>35</sup>Y. Min Nam, J. Huh, and W. Ho Jo, "Optimization of thickness and morphology of active layer for high performance of bulk-heterojunction organic solar cells," *Sol. Energy Mater. Sol. Cells* **94**, 1118–1124 (2010).
- <sup>36</sup>M. Biber, Ş. Aydoğan, Z. Çaldıran, B. Çakmak, T. Karacalı, and A. Türit, "The influence of annealing temperature and time on the efficiency of pentacene: PTCDI organic solar cells," *Results Phys.* **7**, 3444–3448 (2017).
- <sup>37</sup>M. Nagai, W. Gao, W. Huang, H. Yamamoto, and Y. Yoshida, "Effect of drying time on morphology and photovoltaic characteristics of polymer solar cells of bis-PCBM/P3HT composites," *ECS J. Solid State Sci. Technol.* **5**, Q244–Q252 (2016).
- <sup>38</sup>S. Suttty, G. Williams, and H. Aziz, "Role of the donor material and the donor-acceptor mixing ratio in increasing the efficiency of Schottky junction organic solar cells," *Org. Electron.* **14**, 2392–2400 (2013).
- <sup>39</sup>P. K. Shin, P. Kumar, A. Kumar, S. Kannappan, and S. Ochiai, "Effects of organic solvents for composite active layer of PCDTBT/PC 71BM on characteristics of organic solar cell devices," *Int. J. Photoenergy* **2014**, 1.
- <sup>40</sup>C. Müller, T. A. M. Ferenczi, M. Campoy-Quiles, J. M. Frost, D. D. C. Bradley, P. Smith, N. Stingelin-Stutzmann, and J. Nelson, "Binary organic photovoltaic blends: A simple rationale for optimum compositions," *Adv. Mater.* **20**, 3510–3515 (2008).
- <sup>41</sup>Y. Jouane, S. Colis, G. Schmerber, C. Leuvrey, A. Dinia, P. Lévêque, T. Heiser, and Y.-A. Chapuis, "Annealing treatment for restoring and controlling the interface morphology of organic photovoltaic cells with interfacial sputtered ZnO films on P3HT:PCBM active layers," *J. Mater. Chem.* **22**, 1606–1612 (2012).
- <sup>42</sup>M. Campoy-Quiles, T. Ferenczi, T. Agostinelli, P. G. Etchegoin, Y. Kim, T. D. Anthopoulos, P. N. Stavrinou, D. D. C. Bradley, and J. Nelson, "Morphology evolution via self-organization and lateral and vertical diffusion in polymer:fullerene solar cell blends," *Nat. Mater.* **7**, 158–164 (2008).
- <sup>43</sup>L. F. Drummy, R. J. Davis, D. L. Moore, M. Durstock, R. A. Vaia, and J. W. P. Hsu, "Molecular-scale and nanoscale morphology of P3HT:PCBM bulk heterojunctions: Energy-filtered TEM and low-dose HREM," *Chem. Mater.* **23**, 907–912 (2011).
- <sup>44</sup>E. Verploegen, R. Mondal, C. J. Bettinger, S. Sok, M. F. Toney, and Z. Bao, "Effects of thermal annealing upon the morphology of polymer-fullerene blends," *Adv. Funct. Mater.* **20**, 3519–3529 (2010).
- <sup>45</sup>D. E. Motaung, G. F. Malgas, S. S. Nkosi, G. H. Mhlongo, B. W. Mwakikunga, T. Malwela, C. J. Arendse, T. F. G. Muller, and F. R. Cummings, "Comparative study: The effect of annealing conditions on the properties of P3HT:PCBM blends," *J. Mater. Sci.* **48**, 1763–1778 (2013).
- <sup>46</sup>D. Yokoyama, Z. Qiang Wang, Y.-J. Pu, K. Kobayashi, J. Kido, and Z. Hong, "High-efficiency simple planar heterojunction organic thin-film photovoltaics with horizontally oriented amorphous donors," *Sol. Energy Mater. Sol. Cells* **98**, 472–475 (2012).
- <sup>47</sup>O. Oklobia and T. S. Shafai, "A quantitative study of the formation of PCBM clusters upon thermal annealing of P3HT/PCBM bulk heterojunction solar cell," *Sol. Energy Mater. Sol. Cells* **117**, 1–8 (2013).
- <sup>48</sup>K. Kim, J. Liu, M. A. G. Namboothiry, and D. L. Carroll, "Roles of donor and acceptor nanodomains in 6% efficient thermally annealed polymer photovoltaics," *Appl. Phys. Lett.* **90**, 163511 (2007).
- <sup>49</sup>L. Li, G. Lu, S. Li, H. Tang, and X. Yang, "Epitaxy-assisted creation of PCBM nanocrystals and its application in constructing optimized morphology for bulk-heterojunction polymer solar cells," *J. Phys. Chem. B* **112**, 15651–15658 (2008).
- <sup>50</sup>D. Yu *et al.*, "Adhesion in flexible organic and hybrid organic/inorganic light emitting device and solar cells," *J. Appl. Phys.* **116**, 074506 (2014).
- <sup>51</sup>B. Agyei-Tuffour *et al.*, "Pressure effects on interfacial surface contacts and performance of organic solar cells," *J. Appl. Phys.* **122**, 205501 (2017).
- <sup>52</sup>J. Du *et al.*, "Pressure-assisted fabrication of organic light emitting diodes with MoO<sub>3</sub> hole-injection layer materials," *J. Appl. Phys.* **115**, 233703 (2014).
- <sup>53</sup>O. V. Oyelade *et al.*, "Pressure-assisted fabrication of perovskite solar cells," *Sci. Rep.* **10**, 7183 (2020).
- <sup>54</sup>J. Asare *et al.*, "Cold welding of organic light emitting diode: Interfacial and contact models," *AIP Adv.* **6**, 065125 (2016).
- <sup>55</sup>S. A. Adeniji, J. Cromwell, D. O. Oyewole, O. V. Oyelade, R. K. Koech, D. M. Sanni, O. K. Oyewole, B. Babatope, and W. O. Soboyejo, "Pressure-assisted fabrication of perovskite light emitting devices," *AIP Adv.* **11**, 025112 (2021).
- <sup>56</sup>D. G. Cooke, F. C. Krebs, and P. U. Jepsen, "Direct observation of sub-100 fs mobile charge generation in a polymer-fullerene film," *Phys. Rev. Lett.* **108**, 056603 (2012).
- <sup>57</sup>N. Banerji, S. Cowan, E. Vauthey, and A. J. Heeger, "Ultrafast relaxation of the poly(3-hexylthiophene) emission spectrum," *J. Phys. Chem. C* **115**, 9726–9739 (2011).

- <sup>58</sup>S. K. Pal, T. Kesti, M. Maiti, F. Zhang, O. Inganäs, S. Hellström, M. R. Andersson, F. Oswald, F. Langa, T. Österman, T. Pascher, A. Yartsev, and V. Sundström, "Geminate charge recombination in polymer/fullerene bulk heterojunction films and implications for solar cell function," *J. Am. Chem. Soc.* **132**, 12440–12451 (2010).
- <sup>59</sup>P. D. Cunningham and L. M. Hayden, "Carrier dynamics resulting from above and below gap excitation of P3HT and P3HT/PCBM investigated by optical-pump terahertz-probe spectroscopy," *J. Phys. Chem. C* **112**, 7928–7935 (2008).
- <sup>60</sup>X. Ai, M. C. Beard, K. P. Knutsen, S. E. Shaheen, G. Rumbles, and R. J. Ellingson, "Photoinduced charge carrier generation in a poly(3-hexylthiophene) and methanofullerene bulk heterojunction investigated by time-resolved terahertz spectroscopy," *J. Phys. Chem. B* **110**, 25462–25471 (2006).
- <sup>61</sup>M. A. Faist, T. Kirchartz, W. Gong, R. S. Ashraf, I. McCulloch, J. C. de Mello, N. J. Ekins-Daukes, D. D. C. Bradley, and J. Nelson, "Competition between the charge transfer state and the singlet states of donor or acceptor limiting the efficiency in polymer: Fullerene solar cells," *J. Am. Chem. Soc.* **134**, 685–692 (2012).
- <sup>62</sup>J. Piris, T. E. Dykstra, A. A. Bakulin, P. H. M. V. Loosdrecht, W. Knulst, M. T. Trinh, J. M. Schins, and L. D. A. Siebbeles, "Photogeneration and ultrafast dynamics of excitons and charges in P3HT/PCBM blends," *J. Phys. Chem. C* **113**, 14500–14506 (2009).
- <sup>63</sup>G. Li *et al.*, "Equilibrium and non-equilibrium free carrier dynamics in 2D Ti<sub>3</sub>C<sub>2</sub>T<sub>x</sub> MXenes: THz spectroscopy study," *2D Mater.* **5**, 035043 (2018).
- <sup>64</sup>G. Li, V. Natu, T. Shi, M. W. Barsoum, and L. V. Titova, "Two-dimensional MXenes Mo<sub>2</sub>Ti<sub>2</sub>C<sub>3</sub>T<sub>z</sub> and Mo<sub>2</sub>TiC<sub>2</sub>T<sub>z</sub>: Microscopic conductivity and dynamics of photoexcited carriers," *ACS Appl. Energy Mater.* **3**, 1530–1539 (2020).
- <sup>65</sup>K. T. Butler, B. J. Dringoli, L. Zhou, P. M. Rao, A. Walsh, and L. V. Titova, "Ultrafast carrier dynamics in BiVO<sub>4</sub> thin film photoanode material: Interplay between free carriers, trapped carriers and low-frequency lattice vibrations," *J. Mater. Chem. A* **4**, 18516–18523 (2016).
- <sup>66</sup>T. Tong *et al.*, "Adhesion in organic electronic structures," *J. Appl. Phys.* **106**, 083708 (2009).
- <sup>67</sup>Y. Cao, C. Kim, S. R. Forrest, and W. Soboyejo, "Effects of dust particles and layer properties on organic electronic devices fabricated by stamping," *J. Appl. Phys.* **98**, 033713 (2005).
- <sup>68</sup>W. O. Akande, Y. Cao, N. Yao, and W. Soboyejo, "Adhesion and the cold welding of gold-silver thin films," *J. Appl. Phys.* **107**, 043519 (2010).
- <sup>69</sup>A. Monshi, M. R. Foroughi, and M. R. Monshi, "Modified Scherrer equation to estimate more accurately nano-crystallite size using XRD," *World J. Nano Sci. Eng.* **02**, 154–160 (2012).
- <sup>70</sup>Y. Yao, H. Dong, and W. Hu, "Ordering of conjugated polymer molecules: Recent advances and perspectives," *Polym. Chem.* **4**, 5197–5205 (2013).
- <sup>71</sup>P. H. Chu *et al.*, "Toward precision control of nanofiber orientation in conjugated polymer thin films: Impact on charge transport," *Chem. Mater.* **28**, 9099–9109 (2016).
- <sup>72</sup>B. Y. Kadem, A. K. Hassan, and W. Cranton, "Enhancement of power conversion efficiency of P3HT:PCBM solar cell using solution processed Alq<sub>3</sub> film as electron transport layer," *J. Mater. Sci.: Mater. Electron.* **26**, 3976–3983 (2015).
- <sup>73</sup>M.-J. Sher, J. A. Bartelt, T. M. Burke, A. Salleo, M. D. McGehee, and A. M. Lindenberg, "Time- and temperature-independent local carrier mobility and effects of regioregularity in polymer-fullerene organic semiconductors," *Adv. Electron. Mater.* **2**, 1500351 (2016).
- <sup>74</sup>O. Esenturk, J. S. Melinger, and E. J. Heilweil, "Terahertz mobility measurements on poly-3-hexylthiophene films: Device comparison, molecular weight, and film processing effects," *J. Appl. Phys.* **103**, 023102 (2008).
- <sup>75</sup>K. Ohta, S. Tokonami, K. Takahashi, Y. Tamura, H. Yamada, and K. Tominaga, "Probing charge carrier dynamics in porphyrin-based organic semiconductor thin films by time-resolved THz spectroscopy," *J. Phys. Chem. B* **121**, 10157–10165 (2017).
- <sup>76</sup>P. Parkinson, J. Lloyd-Hughes, M. B. Johnston, and L. M. Herz, "Efficient generation of charges via below-gap photoexcitation of polymer-fullerene blend films investigated by terahertz spectroscopy," *Phys. Rev. B* **78**, 115321 (2008).
- <sup>77</sup>P. Krauspe *et al.*, "Terahertz short-range mobilities in neat and intermixed regions of polymer:fullerene blends with controlled phase morphology," *J. Mater. Chem. A* **6**, 22301–22309 (2018).
- <sup>78</sup>C. S. Ponseca *et al.*, "Electron and hole contributions to the terahertz photoconductivity of a conjugated polymer: Fullerene blend identified," *J. Phys. Chem. Lett.* **3**, 2442–2446 (2012).
- <sup>79</sup>G. Lanzani, *Photophysics of Molecular Materials; From Single Molecules to Single Crystals* (Scitech Book News, 2006), Vol. 583.
- <sup>80</sup>P. U. Jepsen, D. G. Cooke, and M. Koch, "Terahertz spectroscopy and imaging—Modern techniques and applications," *Laser Photonics Rev.* **5**, 124–166 (2011).
- <sup>81</sup>N. V. Smith, "Classical generalization of the Drude formula for the optical conductivity," *Phys. Rev. B* **64**(15), 155106 (2001).
- <sup>82</sup>T. L. Cocker *et al.*, "Microscopic origin of the Drude-Smith model," *Phys. Rev. B* **96**, 205439 (2017).
- <sup>83</sup>J. E. Northrup, "Atomic and electronic structure of polymer organic semiconductors: P3HT, PQT, and PBTTT," *Phys. Rev. B* **76**, 245202 (2007).
- <sup>84</sup>B. Agyei-Tuffour *et al.*, "Influence of pressure on contacts between layers in organic photovoltaic cells," *Adv. Mater. Res.* **1132**, 204–216 (2015).